17. P. C. Clark, S. C. O. Glover, R. S. Klessen, *Astrophys. J.* **672**, 757 (2008).
18. M. N. Machida, K. Omukai, T. Matsumoto, S.-i. Inutsuka, *Astrophys. J.* **677**, 813 (2008).
19. V. Bromm, P. S. Coppi, R. B. Larson, *Astrophys. J.* **527**, L5 (1999).
20. B. W. O'Shea *et al*., in *Adaptive Mesh Refinement: Theory and Applications*, T. Plewa, T. Linde, G. Weirs, Eds. (Springer-Verlag, Berlin, 2004).
21. Detailed simulation parameters and methods are available as supporting material on *Science* Online.
22. N. Yoshida, T. Abel, L. Hernquist, N. Sugiyama, *Astrophys. J.* **592**, 645 (2003).
23. E. C. Ostriker, *Astrophys. J.* **513**, 252 (1999).
24. K. Omukai, Y. Yoshii, *Astrophys. J.* **599**, 746 (2003).
25. I. Hachisu, J. E. Tohline, Y. Eriguchi, *Astrophys. J. Suppl. Ser.* **66**, 315 (1988).
26. I. Hachisu, J. E. Tohline, Y. Eriguchi, *Astrophys. J.* **323**, 592 (1987).
27. T. Abel, J. H. Wise, G. L. Bryan, *Astrophys. J.* **659**, L87 (2007).
28. J. Tumlinson, *Astrophys. J.* **641**, 1 (2006).
29. B. W. O'Shea, T. Abel, D. Whalen, M. L. Norman, *Astrophys. J.* **628**, L5 (2005).
30. J. H. Wise, T. Abel, *Astrophys. J.* **685**, 40 (2008).
31. B. W. O'Shea, M. L. Norman, *Astrophys. J.* **673**, 14 (2008).
32. We thank V. Bromm, G. Bryan, A. Escala, S. Glover, C. McKee, J. Oishi, B. Smith, J. Tumlinson, and N. Yoshida for useful discussions. This work was partially supported by the U.S. Department of Energy (DOE) contract to Stanford Linear Accelerator Center no. DE-AC02-76SF00515, NASA Astrophysics Theory and Fundamental Physics grant NNX08AH26G, and NSF AST-0807312. B.W.O. and M.J.T. carried out this work in part under the auspices of the National Nuclear Security Administration of the DOE at Los Alamos National Laboratory (LANL) under contract no. DE-AC52-06NA25396. B.W.O. was partially supported by a LANL Director's Postdoctoral Fellowship (DOE LDRD grant 20051325PRD4).

Supporting Online Material
www.sciencemag.org/cgi/content/full/1173540/DC1
Materials and Methods
Table S1
References

13 March 2009; accepted 15 June 2009
Published online 9 July 2009;
10.1126/science.1173540
Include this information when citing this paper.

Water and the Oxidation State of Subduction Zone Magmas

Katherine A. Kelley[1]*† and Elizabeth Cottrell[2]*

Mantle oxygen fugacity exerts a primary control on mass exchange between Earth's surface and interior at subduction zones, but the major factors controlling mantle oxygen fugacity (such as volatiles and phase assemblages) and how tectonic cycles drive its secular evolution are still debated. We present integrated measurements of redox-sensitive ratios of oxidized iron to total iron ($Fe^{3+}/\Sigma Fe$), determined with Fe K-edge micro–x-ray absorption near-edge structure spectroscopy, and pre-eruptive magmatic H_2O contents of a global sampling of primitive undegassed basaltic glasses and melt inclusions covering a range of plate tectonic settings. Magmatic $Fe^{3+}/\Sigma Fe$ ratios increase toward subduction zones (at ridges, 0.13 to 0.17; at back arcs, 0.15 to 0.19; and at arcs, 0.18 to 0.32) and correlate linearly with H_2O content and element tracers of slab-derived fluids. These observations indicate a direct link between mass transfer from the subducted plate and oxidation of the mantle wedge.

Plate tectonics leads to a two-way geochemical exchange between Earth's interior and exterior. This process is driven by the formation of new oceanic crust by mantle melting at mid-ocean ridges, hydration and oxidative alteration of oceanic crust as it transits the seafloor, and the subsequent return of hydrated oxidized oceanic crust to the deep Earth at subduction zones (Fig. 1A) (*1*, *2*). How this exchange has affected the oxygen fugacity of the mantle spatially (*3*) and over time (*2*, *4*, *5*) remains unclear. Many lines of evidence point to oxidizing conditions in arc peridotites and magmas (*1*, *6*), but a quantitative link between oxidation state and the subduction process, although intuitive, has not been established. Here we provide coupled measurements of the redox-sensitive $Fe^{3+}/\Sigma Fe$ ratio and magmatic H_2O concentrations at the same spatial resolution in a global suite of undegassed basaltic glasses, in order to determine the current oxidation condition of the mantle as a function of tectonic regime.

The ratio of oxidized iron to total iron [$Fe^{3+}/\Sigma Fe = Fe^{3+}/(Fe^{3+} + Fe^{2+})$] in primary, mantle-derived basaltic melts reflects mantle oxygen fugacity, provided that magmas experience minimal modification as they ascend to the surface (*1*, *6*–*8*). Melts may, however, be oxidized by crustal assimilation, crystallization, or degassing during ascent (*3*, *8*, *9*). Interpretation of bulk measurements of $Fe^{3+}/\Sigma Fe$ ratios in lavas (for example, by wet chemistry or Mössbauer spectroscopy) can be complicated because many rock samples, even at small scales, are mixtures of crystals and glass that may not represent true magmatic liquids. Lavas erupted on land also extensively degas, which alters their primary $Fe^{3+}/\Sigma Fe$ ratios (*9*). Submarine pillow rim glasses and melt inclusions (Fig. 1), however, can preserve primitive, minimally degassed magmatic liquids (*10*, *11*).

We used synchrotron-based Fe K-edge micro–x-ray absorption near-edge structure (μ-XANES) spectroscopy to derive $Fe^{3+}/\Sigma Fe$ ratios from the valence-sensitive pre-edge feature corresponding to the $1s \rightarrow 3d$ electronic transition (*12*). The area-weighted average energy of the baseline-subtracted pre-edge feature (the centroid) shifts in energy as a function of Fe oxidation state in basaltic glass (*13*) (Fig. 2A). Natural basalt powders were equilibrated over 16 oxygen fugacities, between –3.5 and +4.5 log units relative to the quartz-fayalite-magnetite (QFM) buffer, to create a suite of calibration glasses of known $Fe^{3+}/\Sigma Fe$ ratios, independently determined by Mössbauer spectroscopy (*14*). Over this compositional range, neither H_2O content (*15*) nor basalt major or minor element concentrations (*14*) influence the relation between the energy of the area-weighted centroid and $Fe^{3+}/\Sigma Fe$. These reference glasses can be used to extract the $Fe^{3+}/\Sigma Fe$ ratio of basalts from multiple tectonic settings and with varying H_2O content, with a precision of ±0.0045, comparable to that determined by wet chemistry (*14*).

Our samples represent melts from a range of tectonic settings, including global submarine pillow-rim glasses from primitive [>6 weight percent (wt %) MgO] mid-ocean ridge basalts (MORBs) and Mariana Trough back-arc basin basalts (BABBs), as well as basaltic olivine-hosted melt inclusions from one MORB and a global suite of arc volcanoes (Fig. 1) (*12*). Based on μ-XANES spectral

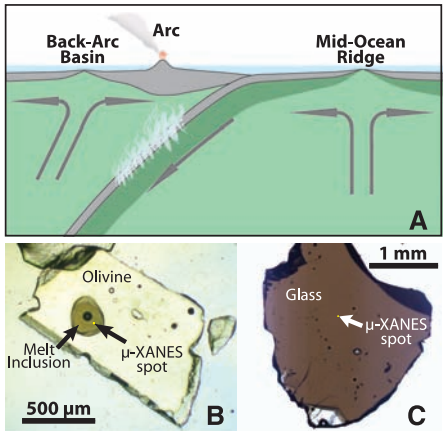

Fig. 1. (**A**) Cartoon showing plate tectonic settings of samples analyzed in this study. Mid-ocean ridges create oceanic crust through mantle upwelling. Hydrated and altered mid-ocean ridge crust is returned to the mantle by subduction, where H_2O released by metamorphic reactions enters the mantle sources of arc volcanoes and back-arc basins. (**B**) Photomicrograph of a double-polished, olivine-hosted arc melt inclusion (sample GUG-DB). The melt inclusion is originally glassy, free of daughter crystals, and contains a single vapor bubble caused by the contraction of the glass upon cooling. The size of the μ-XANES beam is shown for reference. (**C**) Photomicrograph of a wafered back-arc basin glass chip (sample ALV1839-21).

[1]Graduate School of Oceanography, University of Rhode Island, Narragansett, RI 02882, USA. [2]National Museum of Natural History, Smithsonian Institution, Washington, DC 20560, USA.

*These authors contributed equally to this work.
†To whom correspondence should be addressed. E-mail: kelley@gso.uri.edu

analysis, the $Fe^{3+}/\Sigma Fe$ ratio increases from the MORB (0.13 to 0.17) to BABB (0.15 to 0.19) to arc samples (0.18 to 0.32 (Fig. 2B and table S1), which is consistent with evidence that arc magmas are more oxidized than MORBs (*1*, *6*) and contrary to models based on V/Sc ratios (*3*).

Pre-eruptive magmatic concentrations of volatiles (such as H_2O) are also known to vary with tectonic setting, and specifically to increase at subduction zones (*10*, *11*). New measurements of the dissolved H_2O, CO_2, and S concentrations of basaltic glasses were also conducted, either by ion microprobe, following the methods of Hauri (*16*), or by Fourier transform infrared spectroscopy (FTIR) and electron microprobe, using the methods of Luhr (*10*), and were used in conjunction with previously published volatile data (*12*). These results show that magmatic H_2O content increases from MORBs (0.14 to 0.49 wt %) to BABBs (0.57 to 1.89 wt %) to arcs [2.23 to 5.39 wt %; except in one sample from an arc volcano that is known to be H_2O-poor (*17*)]. The oxidation state of Fe in the basaltic melts increases linearly with magmatic H_2O concentrations (Fig. 3). The high H_2O contents of subduction zone magmas have long been expected to relate to oxidized magmas and mantle sources (*1*, *6*, *18*), but these data provide a direct quantitative correlation between $Fe^{3+}/\Sigma Fe$ and water content in global basaltic melts. If the movement of volatiles from the subducted plate into the arc mantle can be linked to changes in Fe oxidation state, then the subduction process may play a central role in changing the mantle oxygen fugacity both across modern tectonic settings and throughout Earth history.

Shallow magmatic processes could cause linear correlations between $Fe^{3+}/\Sigma Fe$ ratios and H_2O concentrations that are unrelated to the properties of the mantle source. Melt oxidation could occur through losses of some S species (such as H_2S) and H_2 driven by degassing or diffusion (*8*), but this would create an inverse relation between volatile content (such as H_2O) and $Fe^{3+}/\Sigma Fe$ ratio. We also excluded glasses showing evidence of H_2O degassing (low concentrations of earlier-degassing CO_2 or S). Small increases in $Fe^{3+}/\Sigma Fe$ ratios and H_2O contents are expected (and are observed within the MORB glasses) because Fe^{3+} and H_2O are incompatible in early-crystallizing olivine, whereas Fe^{2+} is compatible. The trajectories of both $Fe^{3+}/\Sigma Fe$ ratios and H_2O concentrations relative to MgO content, however, indicate that olivine fractional crystallization cannot explain the observed relation between Fe oxidation state and H_2O in BABBs and arc glasses. The melt inclusion samples could also have been modified by post-entrapment crystallization of olivine or diffusive loss of Fe^{2+}. Both of these processes can be detected, and the compositions can be corrected through analysis of melt compositions relative to their olivine hosts (*12*). In cases where Fe-Mg disequilibrium between a melt inclusion and its host olivine was evident, either equilibrium olivine or Fe^{2+} was added incrementally to each melt composition until equilibrium with the host olivine was achieved. On average, post-entrapment corrections resulted in <8% change in $Fe^{3+}/\Sigma Fe$ (table S2). Moreover, $Fe^{3+}/\Sigma Fe$ and H_2O measured on a MORB melt inclusion and the glass exterior to its olivine host directly overlap, suggesting that processes specific to melt inclusions are not the primary cause of the trend.

Rather than shallow or sample-specific processes, melt oxidation appears to be linked to the composition of the mantle source, an idea that is supported by trace element variations. For example, the ratio of Ba concentration (an element that is highly mobile in aqueous fluids) to La concentration (an element that is fluid-immobile) is a proxy for the influence of slab-derived fluid on the composition of the sub-arc mantle source. In the basalt samples from the Mariana arc and back-arc basin, Ba/La ratios of lavas (*12*) progressively increase with increasing $Fe^{3+}/\Sigma Fe$ ratios (Fig. 4 and table S3). Because the Ba/La ratio is minimally influenced by magmatic processes, it is considered a true reflection of the mantle source that gave rise to a given basalt. Covariation of the Ba/La ratio with $Fe^{3+}/\Sigma Fe$ thus suggests that oxidation is directly related to the addition of H_2O from the subducted slab.

The relation between H_2O, trace elements sensitive to slab additions, and Fe oxidation state requires that slab-derived fluids be directly linked to the oxidation process. The slope of the observed trend in $Fe^{3+}/\Sigma Fe$ ratio versus H_2O concentration indicates the magnitude of magmatic oxidation associated with the addition of fluids from the subducted plate. A simple linear regression of the global data yields a slope of 0.026 (that is, basalt $Fe^{3+}/\Sigma Fe$ increases on average by this amount with each weight % increase in magmatic H_2O). Arc melt inclusion data show more variation relative to the tightly correlated MORB and BABB glasses, which internally give a slope of 0.018. The scatter in the arc data probably reflects the geographical diversity of the arc samples, because each volcano samples a distinct combination of slab characteristics (such as plate age or sediment pile) and mantle inputs. Differing extents of fractional crystallization will also create small variations in both H_2O concentration and $Fe^{3+}/\Sigma Fe$ ratio, but we emphasize that such variability is minor relative to the observed trend.

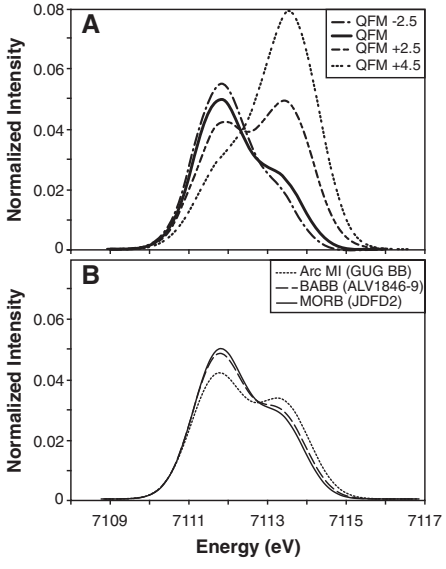

Fig. 2. Comparison of edge-step–normalized, baseline-subtracted, pre-edge μ-XANES spectra for basaltic glasses. The relative intensities of the two pre-edge peaks are diagnostic of the oxidation state of Fe in the glass. (**A**) Baseline-subtracted spectra for reference glasses of All-92-29-1 (*12*), equilibrated at QFM − 2.5 (dash-dot line), QFM (solid line), QFM + 2.5 (dash–double-dot line), and QFM + 4.5 (triple-dot line). (**B**) Baseline-subtracted spectra for natural samples, including a MORB glass (JDFD2, thin solid line), a BABB glass (ALV1846-9, thin dashed line), and an arc melt inclusion (GUG BB, thin dotted line).

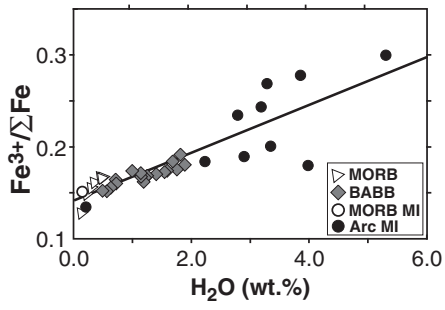

Fig. 3. Plot of measured H_2O concentrations versus $Fe^{3+}/\Sigma Fe$ determined by μ-XANES for MORB and BABB glasses, and olivine-hosted melt inclusions (MIs) from MORBs and global arc volcanoes. $Fe^{3+}/\Sigma Fe$ in MIs have been corrected for post-entrapment olivine crystallization or outward Fe^{2+} diffusion to place the melt compositions in equilibrium with the host olivine. Data for H_2O are published FTIR data from the literature or are FTIR or ion microprobe data from this study (*12*). Symbols exceed the size of the error bars in $Fe^{3+}/\Sigma Fe$ [±0.0045 (1σ)]. The solid line is a least-squares linear regression through all of the data, with equation $y = 0.026x + 0.14$ [correlation coefficient (r^2) = 0.72]. When only MORB and BABB data are used, linear regression gives $y = 0.018 + 0.14$ ($r^2 = 0.65$).

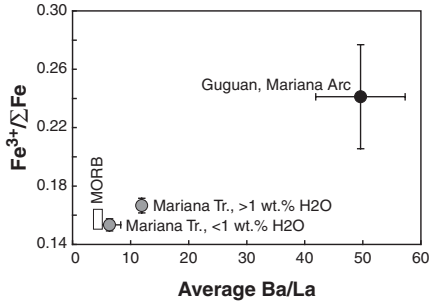

Fig. 4. Plot of average Ba/La ratio versus measured $Fe^{3+}/\Sigma Fe$ for MORBs, and subsets of BABB and arc basalts from the Mariana subduction zone. See supporting online material for sources of the Ba/La ranges for MORBs, the Guguan volcano, and the Mariana Trough. MORB and BABB glasses with 7.0 to 7.5 wt % MgO were used to average $Fe^{3+}/\Sigma Fe$.

Our data implicate the subduction process in the generation of magmas at higher oxygen fugacities than those of MORBs. If the mantle were equally reducing beneath ridges, back-arc basins, and arcs, then primitive undegassed basalts should have similar $Fe^{3+}/\Sigma Fe$ ratios in all three tectonic settings. At subduction zones, however, hydrated oxidized oceanic crust from Earth's surface is thrust into the mantle, where it contributes H_2O-rich fluids and/or melts, and its oxidized signature, to the mantle sources of arc volcanoes and back-arc spreading ridges (Fig. 1A). Indeed, undegassed BABBs and arc melts are systematically more oxidized than MORBs (Fig. 3). Differences between these tectonic regions may actually be underestimated, because H_2O acts to increase the extent of melting, leading to trace-element dilution at high melt fractions (*11*, *19*). If Fe^{3+} behaves strictly as an incompatible element, $Fe^{3+}/\Sigma Fe$ is expected to be higher in MORBs, where melt fractions are low, and to be lower in BABBs and arc basalts, where melt fractions are higher. On the other hand, H_2O may lower the activity coefficient of FeO during mantle melting, which could increase $Fe^{3+}/\Sigma Fe$ in hydrous mantle melts (*11*, *20*, *21*); however, experimental studies are not conclusive (*21*, *22*) and the effect of H_2O is likely to be minor relative to that of temperature (*21*).

Although H_2O concentrations and the oxidation state of Fe correlate linearly in these basalts, H_2O is not required to be the cause of oxidation. Water acts as an efficient oxidizing agent in many terrestrial environments, but not in Earth's upper mantle (*23*). For H_2O alone to play this role requires the efficient dissociation of H_2 from O^{2-}, followed by the efficient removal of H_2. Magmatic oxidation due to loss of H_2 may be responsible for oxidizing basalt pillow cores (*8*) at low pressure, but whether H_2O can dissociate to liberate H_2 in the mantle wedge remains controversial (*18*, *23*). The relation between Fe oxidation state and magmatic H_2O content at subduction zones may instead arise indirectly, as a consequence of the oxidized condition of the subducted oceanic lithosphere. Iron in marine sediments is highly oxidized [$Fe^{3+}/\Sigma Fe$ = ~82% (*2*)], and hydrothermal alteration of both basalt and peridotite results in a net oxidation of the oceanic lithosphere through the formation of Fe-oxyhydroxides and magnetite and the release of H_2 to the ocean (*2*, *24*). The subducting plate thus enters the mantle at intrinsically higher oxygen fugacity and clearly supplies the H_2O flux into the mantle wedge, but the associated transfer of the oxidized signature from the slab is poorly understood.

Dilute aqueous fluids are inefficient carriers of of Fe^{3+} (*25*), but as slab-derived components become more acidic, more saline, or more melt-like, Fe^{3+} may become highly mobile, as has been shown for other trivalent fluid-immobile elements (*26*, *27*). Transporting all of the Fe^{3+} that we observe in arc basalts in excess of MORBs directly from the slab into the mantle wedge would therefore require that slab-derived H_2O-rich components be hypersaline brines, supercritical fluids, or silicate melts of subducted sediments or the basaltic plate (*26*–*28*). Alternatively, fluid-mobile elements such as S could oxidize the mantle wedge of subduction zones without requiring direct transport of Fe^{3+}. If the intrinsic oxygen fugacity of fluids released from the descending slab is sufficiently high to carry S as sulfate (S^{6+}), then 1 mol of S has the potential to oxidize 8 mol of Fe^{2+} as sulfate in the fluid is reduced to form sulfide (S^{2-}) in the mantle. Sulfur reduction will take place provided that the oxygen fugacity of the mantle wedge remains below the sulfur-sulfur oxide buffer, or approximately QFM + 2 (*29*). From this perspective, if hydrous slab-derived components carry sufficient sulfate (*30*), direct addition of Fe^{3+} from the slab may not be required.

References and Notes

1. B. J. Wood, L. T. Bryndzia, K. E. Johnson, *Science* **248**, 337 (1990).
2. C. Lecuyer, Y. Ricard, *Earth Planet. Sci. Lett.* **165**, 197 (1999).
3. C.-T. A. Lee, W. P. Leeman, D. Canil, Z.-X. A. Li, *J. Petrol.* **46**, 2313 (2005).
4. D. Canil, *Earth Planet. Sci. Lett.* **195**, 75 (2002).
5. A. J. Berry, L. V. Danyushevsky, H. S. C. O'Neill, M. Newville, S. R. Sutton, *Nature* **455**, 960 (2008).
6. I. J. Parkinson, R. J. Arculus, *Chem. Geol.* **160**, 409 (1999).
7. V. C. Kress, I. S. E. Carmichael, *Contrib. Mineral. Petrol.* **108**, 82 (1991).
8. D. M. Christie, I. S. E. Carmichael, *Earth Planet. Sci. Lett.* **79**, 397 (1986).
9. M. Sato, T. L. Wright, *Science* **153**, 1103 (1966).
10. J. F. Luhr, *Contrib. Mineral. Petrol.* **142**, 261 (2001).
11. E. Stolper, S. Newman, *Earth Planet. Sci. Lett.* **121**, 293 (1994).
12. Materials and methods are available as supporting material on *Science* Online.
13. M. Wilke, G. M. Partzsch, R. Bernhardt, D. Lattard, *Chem. Geol.* **220**, 143 (2005).
14. E. Cottrell, K. A. Kelley, A. T. Lanzirotti, R. A. Fischer, *Chem. Geol.*, in press.
15. R. E. Botcharnikov, J. Koepke, F. Holtz, C. McCammon, M. Wilke, *Geochim. Cosmochim. Acta* **69**, 5071 (2005).
16. E. Hauri, *Chem. Geol.* **183**, 99 (2002).
17. T. W. Sisson, S. Bronto, *Nature* **391**, 883 (1998).
18. A. D. Brandon, D. S. Draper, *Geochim. Cosmochim. Acta* **62**, 333 (1998).
19. K. A. Kelley *et al.*, *J. Geophys. Res.* **111**, B09208 (2006).
20. I. Kushiro, *J. Petrol.* **13**, 311 (1972).
21. G. A. Gaetani, T. L. Grove, *Contrib. Mineral. Petrol.* **131**, 323 (1998).
22. K. Hirose, T. Kawamoto, *Earth Planet. Sci. Lett.* **133**, 463 (1995).
23. B. R. Frost, C. Ballhaus, *Geochim. Cosmochim. Acta* **62**, 329 (1998).
24. M. E. Berndt, D. E. Allen, W. E. Seyfried, *Geology* **24**, 351 (1996).
25. M. E. Schneider, D. H. Eggler, *Geochim. Cosmochim. Acta* **50**, 711 (1986).
26. M. C. Johnson, T. Plank, *Geochem. Geophys. Geosyst.* **1**, 10.1029/1999GC000014 (1999).
27. R. Kessel, M. W. Schmidt, P. Ulmer, T. Pettke, *Nature* **437**, 724 (2005).
28. C. E. Manning, *Earth Planet. Sci. Lett.* **223**, 1 (2004).
29. M. R. Carroll, M. J. Rutherford, *J. Petrol.* **28**, 781 (1987).
30. P. J. Wallace, *J. Volcanol. Geotherm. Res.* **140**, 217 (2005).

31. Thanks to R. Fischer and D. Kratzmann for beamline assistance and data processing; T. Gooding for sample preparation; A. Logan for electron microprobe assistance; D. Christie, T. Plank, L. Cooper, M. Zimmer, E. Hauri, M. Hirschmann, and C. Langmuir for samples, data, and discussion; and A. Lanzirotti for beamline method development. This work was supported by a Smithsonian Scholarly Studies Grant to E.C., a NSF ADVANCE fellowship to K.K., and NSF awards EAR-0841108 (K.K.) and EAR-0841006 (E.C.). NSF award OCE-0644625 provided curatorial support for marine geological samples at the University of Rhode Island. Beamline X26A is supported by the U.S. Department of Energy (DOE) Geosciences Division (grant DE-FG02-92ER14244 to the University of Chicago, Consortium for Advanced Radiation Sources). Use of the National Synchrotron Light Source was supported by DOE under contract no. DE-AC02-98CH10886.

Supporting Online Material

www.sciencemag.org/cgi/content/full/325/5940/605/DC1
Materials and Methods
Figs. S1 to S4
Tables S1 to S3
References

27 March 2009; accepted 10 June 2009
10.1126/science.1174156

The cAMP Sensor Epac2 Is a Direct Target of Antidiabetic Sulfonylurea Drugs

Chang-Liang Zhang,[1] Megumi Katoh,[1] Tadao Shibasaki,[1] Kohtaro Minami,[1] Yasuhiro Sunaga,[1]* Harumi Takahashi,[1] Norihide Yokoi,[1] Masahiro Iwasaki,[1] Takashi Miki,[1] Susumu Seino[1,2,3]†

Epac2, a guanine nucleotide exchange factor for the small guanosine triphosphatase Rap1, is activated by adenosine 3′,5′-monophosphate. Fluorescence resonance energy transfer and binding experiments revealed that sulfonylureas, widely used antidiabetic drugs, interact directly with Epac2. Sulfonylureas activated Rap1 specifically through Epac2. Sulfonylurea-stimulated insulin secretion was reduced both in vitro and in vivo in mice lacking Epac2, and the glucose-lowering effect of the sulfonylurea tolbutamide was decreased in these mice. Epac2 thus contributes to the effect of sulfonylureas to promote insulin secretion. Because Epac2 is also required for the action of incretins, gut hormones crucial for potentiating insulin secretion, it may be a promising target for antidiabetic drug development.

Epac is a guanine nucleotide exchange factor (GEF) for the Ras-like small guanosine triphosphatases Rap1 and Rap2 that is activated by the direct binding of adenosine 3′,5′-monophosphate (cAMP); two isoforms of Epac (also referred to as cAMP-GEF), Epac1 (cAMP-GEFI) and Epac2 (cAMP-GEFII), have been identified (*1*–*4*). Epac2 mediates the potentiation of

Supporting Online Material to accompany the manuscript,

"Water and the oxidation state of subduction zone magmas" by K.A. Kelley and E. Cottrell

Materials and Methods

Samples

Natural samples analyzed in this study comprise naturally-quenched glass chips from the rims of submarine-erupted pillow lavas and olivine-hosted melt inclusions from subaerially erupted scoria and tephra.

• *Pillow glass chips* presented in this study were provided by D. Christie, C. Langmuir, J. Hawkins, and the Division of Petrology and Volcanology, Department of Mineral Sciences, Smithsonian Institution. MORB glasses used in this study are from a global sampling of Mid-Ocean Ridges, including the Mid-Atlantic ridge, East Pacific rise, Juan de Fuca ridge, and the Galapagos spreading center. Back-arc basin glasses used in this study are from the Mariana trough. Published major, trace, volatile and/or isotope data for these samples are available online via PetDB (www. PetDB.org) and are provided in Supplementary Table 1.

• *Olivine-hosted melt inclusions* presented in this study were provided by personal collections (Kelley), T. Plank, M. Zimmer, and the Division of Petrology and Volcanology, Department of Mineral Sciences, Smithsonian Institution. The global suite of arc volcanoes covered by these samples include the Marianas (Guguan and Sarigan volcanoes), Aleutians (Mt. St. Augustine), Java (Galunggung volcano), Andaman (Barren Island), and Mexico (Paricutín).

Sample Preparation

Glass chips were prepared as double-polished wafers of appropriate thickness to ensure a clear optical path through the glass (usually 30-100 μm). Glass wafers were carefully examined under a petrographic microscope in both plane-polarized light and through crossed polars to identify crystal-free regions and ensure clean glass was available for analysis.

Olivine hosted melt inclusions were hand-picked from mineral separates of volcanic scoria and tephra. Inclusion-hosting olivine crystals were carefully examined before preparation, to ensure that all chosen melt inclusions were made of clear, brown glass, were fully enclosed by the host crystal, and contained no visible secondary crystals. All melt inclusions selected for this study were naturally glassy. None were experimentally re-homogenized. Melt inclusions were prepared as doubly-intersected wafers, providing an exposed glass surface on each side of the wafer and a clear optical path through glass alone, with no interference from the host olivine. This preparation technique is commonly used for FTIR analyses, which also require beam passage through glass only.

μ-XANES Analytical Methods

Micro X-ray Absorption Near Edge Structure (μ-XANES) spectroscopy is a synchrotron-based microbeam analytical method for the analysis of multivalent element speciation in natural and synthetic materials. For this study, μ-XANES analyses were conducted at the Fe K-edge, from 7020-7220 eV, using a 9 x 5 μm x-ray beam, at

beamline X26A, National Synchrotron Light Source, Brookhaven National Laboratory, USA. Data were collected in fluorescence, using a Si (311) monochromator. The pre-edge region from 7110-7118 eV was extracted from each spectrum and simultaneously fit with four functional components: a linear function constrained to have a positive slope and a damped harmonic oscillator function (DHO) were used to fit the baseline of the main Fe absorption edge, and two Gaussians were used to fit the two pre-edge peaks (Fig. S1). The area-weighted average (i.e., the centroid) of the two Gaussians was used as the parameter against which Fe valence state was calibrated. Area-weighted centroid values were corrected for non-linear instrumental energy drift by use of a drift-correcting reference glass analyzed every few samples, with resultant analytical precision of the area-weighted centroid energy, determined on replicate analyses of single glasses, of 0.008 ±0.005 eV. A calibration curve was constructed using experimental glasses of two natural basalt starting compositions, equilibrated at 1 atm over a range of oxygen fugacities expected for natural basalts (i.e., QFM-3.5 to +4.5). $Fe^{3+}/\sum Fe$ is determined with comparable precision to wet chemistry (±0.0045 [1σ] for glasses with ≥8% ferric iron [~QFM-2; (S*1*)]).

The full μ-XANES spectrum of each unknown sample was carefully examined to assess the potential presence of olivine crystals in the beam path. The broad plateau of Fe absorption at high energy develops significant structure when crystals are in the beam path, and the influence of olivine in the spectra is readily identified (Fig. S2). Complete μ-XANES spectra and close-up views of the raw pre-edge region of MORB, BABB, and arc melt inclusion glasses are shown in Figure S3 for comparison (note that these are the raw spectra of the baseline-subtracted spectra shown in Fig. 2).

Post-Entrapment Corrections to Melt Inclusion Compositions

Equilibrium between melt inclusions and their olivine hosts was assessed by separating FeO* in each melt composition into Fe_2O_3 and FeO using the measured $Fe^{3+}/\sum Fe$, and then calculating the olivine in equilibrium with each melt composition using $K_D^{ol\text{-}liq}[Fe/Mg] = 0.3$. The calculated equilibrium olivine was compared with measurements of the host olivine composition for each sample, and any differences were ascribed to post-entrapment processes. If a melt inclusion indicated equilibrium with olivine of lower Fo than the true host, then post-entrapment olivine crystallization was assumed to have occurred. In these cases, equilibrium olivine was added back to the melt compositions in 1% increments, re-calculating the equilibrium olivine at each increment, until the melt indicated equilibrium with the Fo of the host olivine. If a melt inclusion indicated equilibrium with olivine of a higher Fo than the true host, then post-entrapment Fe^{2+} diffusion out of the melt inclusion was assumed to have occurred. In these cases, the FeO concentration of the melt inclusion was increased, and the concentrations of the other major elements proportionally diluted, until the melt indicated equilibrium with the Fo of the host olivine. In most cases, the melt inclusions indicated approximate equilibrium with their olivine hosts (Fig. S4), and the magnitude of post-entrapment modifications was small (on average, <8% difference in $Fe^{3+}/\sum Fe$).

Figure S1

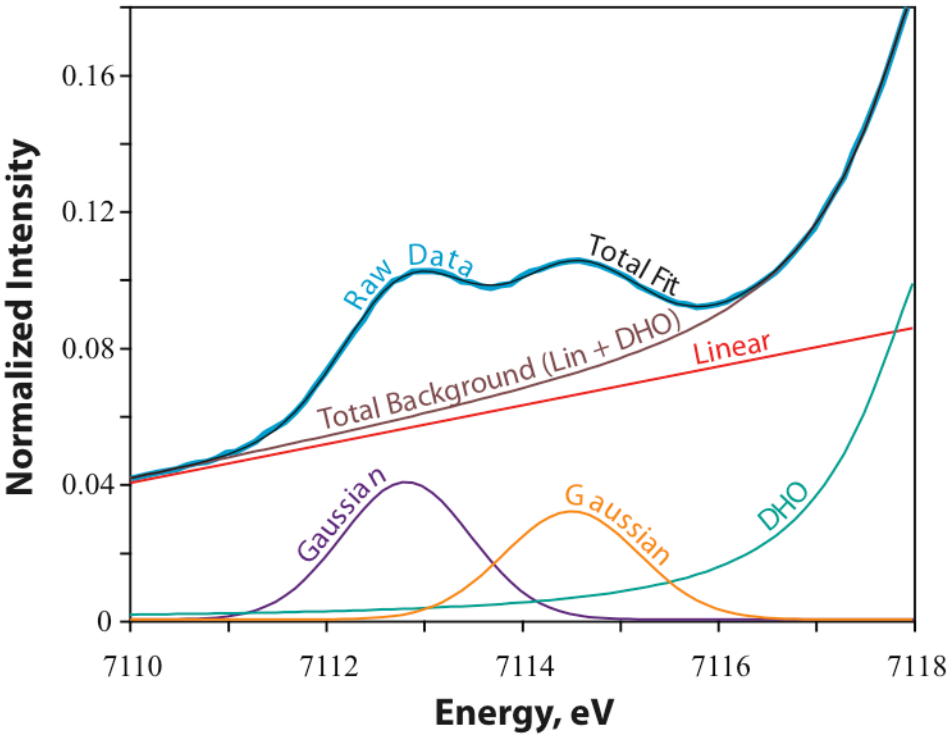

Figure S1. Plot of energy vs. edge-step normalized intensity for the pre-edge region of melt inclusion sample GUG BB, showing the functional components of the model fit to the XANES data. The raw data are shown as the thick, blue line. The model components are shown as thin lines. The Fe-absorption baseline function (brown) is the sum of the linear (red) and damped harmonic oscillator (DHO; green) functions. The pre-edge peaks are fit with two Gaussians (purple and orange). The sum of the four discrete components comprises the total fit (black).

Figure S2

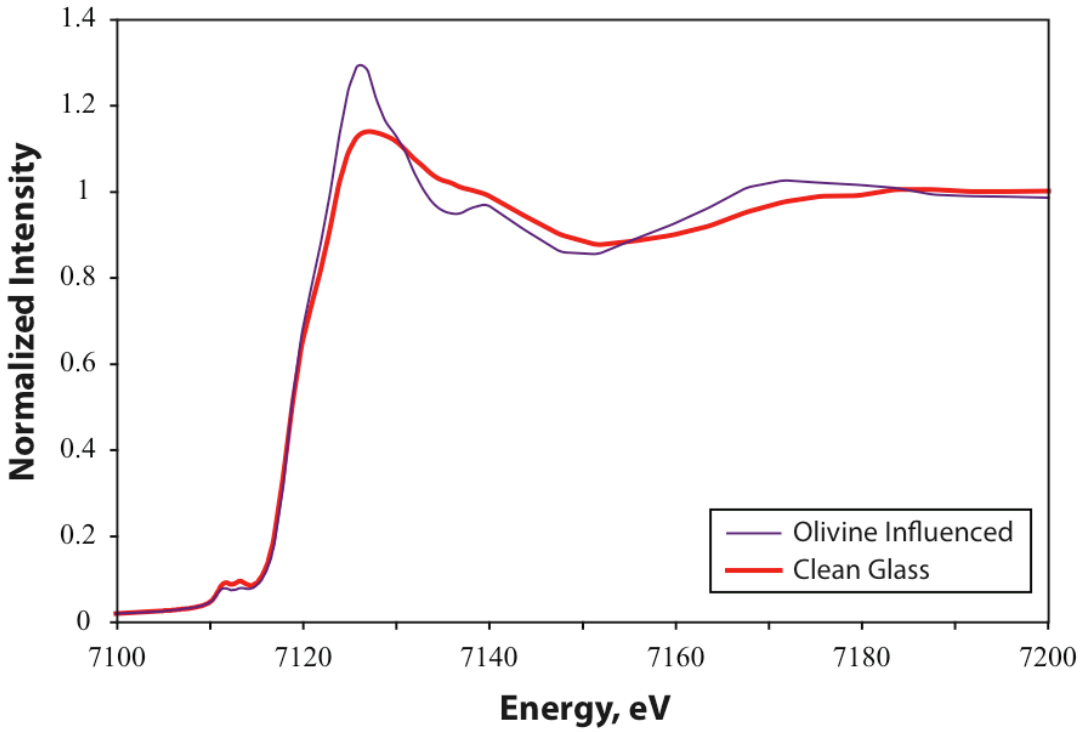

Figure S2. Plot of energy vs. raw edge-step normalized intensity for the full Fe K-edge region showing clean glass and olivine-influenced spectra for melt inclusion sample 2A/22/5/92-A. The olivine-influenced spectrum (thin, purple line) shows significant structure across the edge-step from ~7120-7180 eV, indicative of the influence of a crystal lattice. The glass spectrum (thick, red line) is significantly damped across this region. These spectra have been corrected for instrumental energy drift, following methods outlined in (S*1*).

Figure S3

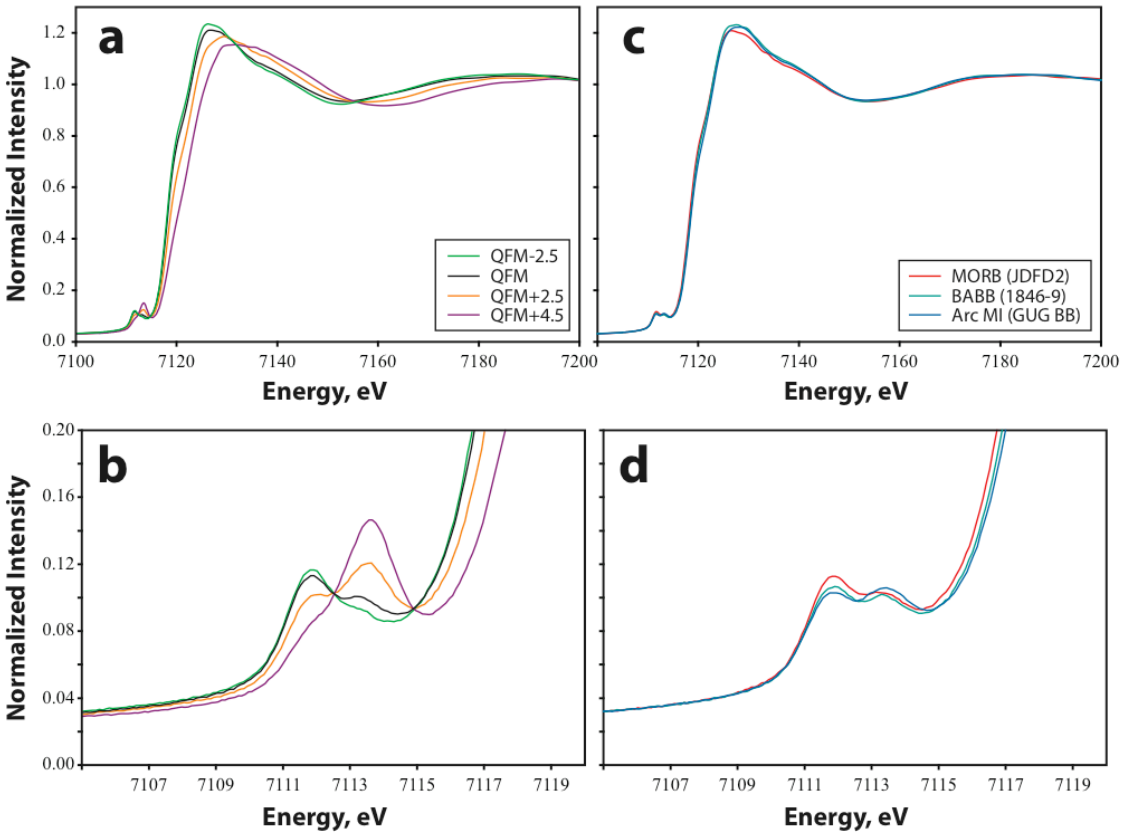

Figure S3. Plots of energy vs. raw edge-step normalized intensity for four reference glasses (a-b) and three natural glass samples (c-d). The reference glasses are experiments on composition AII-92-29-1 (Smithsonian catalog number: 113707-2, volcanic glass collection number: VG2524;(S*2*)), equilibrated at QFM-2.5 (green line), QFM (black line), QFM+2.5 (orange line), and QFM+4.5 (fuschia line), showing (a) full XANES spectra, and (b) the pre-edge region. MORB glass JDFD2 (red), BABB glass ALV1846-9 (green), and arc melt inclusion GUG BB (blue) showing (c) full XANES spectra, and (d) the pre-edge region. These spectra have been corrected for instrumental energy drift, following methods outlined in (S*1*).

Figure S4

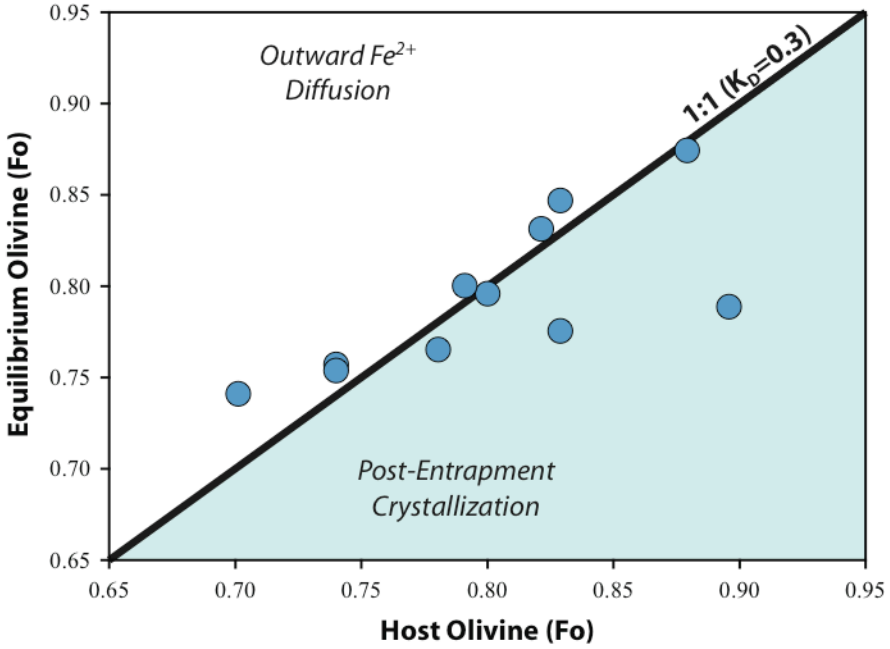

Figure S4. Plot of calculated equilibrium olivine for melt inclusion glasses vs. measured host olivine composition. The thick black line indicates a 1:1 relationship equivalent to equilibrium between a melt inclusion and its host olivine, using $K_D^{ol\text{-}liq}[Fe/Mg] = 0.3$. Samples falling in the shaded region have likely experienced post-entrapment fractional crystallization of olivine. Samples falling in the un-shaded region have likely experienced diffusion of Fe^{2+} out of the melt inclusion since entrapment.

Table S1. Major and volatile element concentrations and $Fe^{+3}/\sum Fe$ ratios for MORB, BABB, and olivine-hosted melt inclusions

Sample Name	Smithsonian Catalog Number / Volcanic Glass Number	PetDB ID	Type	Location	SiO_2	TiO_2	Al_2O_3	FeO*	MnO	MgO	CaO	Na_2O	K_2O	P_2O_5	Total	$Fe^{3+}/\sum Fe$	Host Olivine Fo
EN113_13D-1B [2]		END0113-013-001	MORB glass	East Pacific rise	48.16	1.48	17.17	8.88	0.20	7.91	11.70	3.22	0.02	0.10	98.85	0.15	
ALV 527 1-1 [*S5, S6*]	113811; VG3403	ALV0527-001-001	MORB glass	Mid-Atlantic ridge	48.41	0.69	16.93	9.01		9.48	12.56	2.00	0.07	0.06	99.21	0.13	
CH 6-1 [*S7, S8*]		NHOCHEP-006-001	MORB glass	East Pacific rise	50.48	1.95	14.74	10.42	0.22	6.99	11.04	3.02	0.32	0.21	99.40	0.16	
EN25 6D-3 [*S9, S6*]	116886-3; VG6979	END0025-006-003	MORB glass	Mid-Atlantic ridge	51.50	1.29	14.16	12.20		6.91	11.46	2.07	0.10	0.12	99.81	0.15	
K 10-34 [*S6*]	115191-32; VG4795	KAK1979-010-034	MORB glass	Galapgos spreading center	48.06	0.99	17.33	8.54		8.99	12.02	2.35	0.05	0.07	98.40	0.15	
K 14-3 [*S6*]	115194-3; VG4517	KAK1979-014-003	MORB glass	Galapgos spreading center	51.21	1.76	13.48	11.59		6.19	10.86	2.50	0.17	0.17	97.93	0.17	
K 18-21 [*S6*]	115198-21; VG4550	KAK1979-018-021	MORB glass	Galapgos spreading center	50.72	1.76	13.93	11.18		7.08	10.75	2.33	0.17	0.17	98.09	0.17	
JDFD2 [*S6*]	117354-47; VG7433	DSC1983-002-002	MORB glass	Juan de Fuca ridge	50.95	1.88	13.99	12.22	0.22	6.50	10.96	2.62	0.20	0.22	99.76	0.17	
76-1-1 [*S10, S11*]		WASTUNE-7-076-001-1	BABB glass	Mariana trough	52.79	1.62	15.88	9.48		7.23	10.37	3.48	0.23	0.18	101.26	0.16	
71-1-14 [*S10, S11*]	117358-49; VG10475	WASTUNE-7-071-001-14	BABB glass	Mariana trough	51.70	1.11	16.50	7.72	0.15	6.34	11.70	2.99	0.42	0.20	98.83	0.19	
74-1-1 [*S10, S11*]	117358-60; VG10484	WASTUNE-7-074-001-1	BABB glass	Mariana trough	51.09	1.13	17.83	7.22	0.15	7.72	11.83	2.75	0.30	0.17	100.19	0.17	
46-1-6 [*S10, S11*]	117358-7; VG10428	WASTUNE-7-046-001-6	BABB glass	Mariana trough	51.46	1.12	16.95	7.81	0.15	7.07	11.56	2.70	0.22	0.15	99.19	0.17	
47-1-5 [*S10, S11*]	117358-12; VG10433	WASTUNE-7-047-001-5	BABB glass	Mariana trough	51.22	0.96	16.60	7.53	0.16	7.33	12.12	2.49	0.24	0.13	98.78	0.17	
75-1-2 [*S10, S11*]		WASTUNE-7-075-001-2	BABB glass	Mariana trough	52.30	1.61	16.38	8.38		7.33	10.60	3.27	0.35	0.18	100.40	0.16	
73-2-1 [*S10, S11*]	117358-57; VG10481	WASTUNE-7-073-002-1	BABB glass	Mariana trough	51.90	1.41	17.15	7.82	0.15	6.69	10.53	3.56	0.33	0.18	99.72	0.17	
80-1-3 [*S10, S11*]	117358-74; VG10498	WASTUNE-7-080-001-3	BABB glass	Mariana trough	49.56	0.84	17.93	8.61	0.16	8.60	11.55	2.40	0.35	0.14	100.14	0.15	
82-1-1 [*S10, S11*]	117358-76; VG10500	WASTUNE-7-082-001-1	BABB glass	Mariana trough	51.40	1.27	16.60	7.94	0.16	6.43	11.22	3.07	0.24	0.17	98.50	0.18	
WOK 5-4 [*S10, S12*]		AII0118-14-005-004	BABB glass	Mariana trough	50.67	0.93	17.49	7.20	0.16	7.34	11.86	2.57	0.29	0.12	98.63	0.17	
WOK 10-1 [*S10, S12*]		AII0118-14-010-001	BABB glass	Mariana trough	51.85	1.24	16.15	8.21	0.14	6.60	11.16	2.91	0.26	0.13	98.65	0.17	
WOK 16-2 [*S10, S12*]		AII0118-14-016-002	BABB glass	Mariana trough	51.12	1.53	15.99	9.13	0.17	7.54	10.67	3.12	0.19	0.18	99.64	0.16	
WOK 28-3 [*S10, S12*]		AII0118-14-028-003	BABB glass	Mariana trough	49.95	1.22	17.56	9.22	0.22	7.61	11.14	3.21	0.10	0.13	100.36	0.15	
ALV 1833-11 [*S10, S13*]		ALV1833-011	BABB glass	Mariana trough	51.13	1.04	17.16	7.55	0.15	7.55	11.92	2.86	0.25	0.18	99.79	0.16	
ALV 1839-21 [*S10, S13*]		ALV1839-021	BABB glass	Mariana trough	51.45	1.17	17.84	7.63	0.14	7.47	11.41	2.58	0.27	0.13	100.09	0.17	
ALV 1840-3 [*S10, S12*]		ALV1840-003	BABB glass	Mariana trough	51.83	1.18	16.86	7.99	0.15	6.78	10.66	3.09	0.30	0.13	98.97	0.17	
ALV 1846-9 [*S10, S13*]		ALV1846-009	BABB glass	Mariana trough	49.67	0.57	17.45	7.03	0.16	6.95	13.46	2.07	0.71	0.13	98.20	0.18	
ALV 1846-12 [*S10, S13*]		ALV1846-012	BABB glass	Mariana trough	50.75	1.11	17.30	7.56	0.15	7.00	11.39	2.75	0.40	0.18	98.59	0.17	
108153-A [*S4*]	108153		Arc MI	Paricutin, Mexico	52.48	0.98	16.45	6.64	0.13	4.95	6.90	3.41	1.06	0.40	93.40	0.20	0.83
2A/22/5/92-A [*S14*]	117273-25		Arc MI	Barren Island, Andaman	52.84	1.16	16.36	10.57	0.23	4.36	7.27	2.82	0.65	0.14	96.40	0.20	0.74
2A/22/5/92-B [*S14*]	117273-25		Arc MI	Barren Island, Andaman	51.54	1.18	16.32	10.22	0.25	4.21	7.50	3.95	0.64	0.16	95.97	0.22	0.74
G98-02 [*S15*]			Arc MI	Galunggung, Java	49.25	1.32	20.34	7.40	0.15	3.80	13.04	3.24	0.54	0.15	99.23	0.18	0.90
05AUNY17_1 [*S16*]			Arc MI	Augustine, Aleutians	48.73	0.66	17.19	7.82	0.14	4.45	10.50	2.16	0.54	0.17	92.36	0.32	0.82
GUG BB [2]			Arc MI	Guguan, Marianas	44.61	1.10	17.81	11.53	0.21	5.87	12.10	1.95	0.33	0.10	95.61	0.24	0.79
GUG D [*S17*]			Arc MI	Guguan, Marianas	45.70	0.74	18.01	11.32	0.24	5.44	12.58	1.95	0.30	0.09	96.36	0.27	0.80
GUG DB [2]			Arc MI	Guguan, Marianas	51.99	1.05	14.79	12.56	0.26	4.74	7.79	2.78	0.56	0.13	96.65	0.22	0.70
GUG J-F [*S17*]			Arc MI	Guguan, Marianas	46.01	0.80	18.14	11.80	0.26	4.85	12.50	1.98	0.33	0.04	96.69	0.25	0.78
SA 93-1 [2]			Arc MI	Sarigan, Marianas	53.50	0.55	15.63	7.06	0.14	2.85	10.99	2.13	0.57	0.03	93.46	0.31	0.83
EN113_13D-1B [2]		END0113-013-001	MORB MI	East Pacific rise	48.28	1.20	18.36	7.84	0.14	7.82	12.15	3.25	0.01	0.09	99.14	0.15	0.88

[1] Analyzed by secondary ionization mass spectrometry at the Department of Terrestrial Magnetism, Carnegie Insitution of Washington, following the techniques of Hauri (*S3*).

[2] Analyzed by electron microprobe and/or Fourier Transform Infrared Spetroscopy at the National Museum of Natural History, Smithsonian Institution, following the techniques of Luhr (*S4*).

Table S1 continued. Major and volatile element concentrations and $Fe^{+3}/\sum Fe$ ratios for MORB, BABB, and olivine-hosted melt inclusions

Sample Name	H_2O, wt.% (SIMS [1])	CO_2, ppm (SIMS [1])	S, ppm (SIMS [1])	H_2O, wt.% (FTIR)	CO_2, ppm (FTIR)	H_2O, wt.% (NMNH FTIR [2])	CO_2, ppm (NMNH FTIR [2])	S, ppm (EMP, [2])
EN113_13D-1B [2]						0.14		861
ALV 527 1-1 [*S5, S6*]				0.14				867 [*S18*]
CH 6-1 [*S7, S8*]	0.34	170	1309					
EN25 6D-3 [*S9, S6*]				0.30				
K 10-34 [*S6*]	0.22	177	1059					
K 14-3 [*S6*]	0.48	120	1659					
K 18-21 [*S6*]	0.49	161	1292					
JDFD2 [*S6*]	0.45	252	1670					
76-1-1 [*S10, S11*]				0.73	180			
71-1-14 [*S10, S11*]				1.82	128			
74-1-1 [*S10, S11*]				1.00	112			
46-1-6 [*S10, S11*]				1.41	111			
47-1-5 [*S10, S11*]				1.76	66			
75-1-2 [*S10, S11*]				0.72	227			
73-2-1 [*S10, S11*]				1.15	160			
80-1-3 [*S10, S11*]				0.57	295			
82-1-1 [*S10, S11*]				1.69	109			
WOK 5-4 [*S10, S12*]				1.60	64			
WOK 10-1 [*S10, S12*]				1.14	120			
WOK 16-2 [*S10, S12*]				0.64	184			
WOK 28-3 [*S10, S12*]				0.50	183			
ALV 1833-11 [*S10, S13*]				1.20	102			
ALV 1839-21 [*S10, S13*]				1.21	94			
ALV 1840-3 [*S10, S12*]				1.26	113			
ALV 1846-9 [*S10, S13*]				1.89				370 [*S19*]
ALV 1846-12 [*S10, S13*]				1.55	90			
108153-A [*S4*]						4.00	296	2500
2A/22/5/92-A [*S14*]						2.90	13	790
2A/22/5/92-B [*S14*]						3.36	19	1026
G98-02 [*S15*]	0.21	99	548			0.26		
05AUNY17_1 [*S16*]	5.29	145	4130			5.39		
GUG BB [2]						2.80	176	
GUG D [*S17*]				3.28				1894
GUG DB [2]						2.23		307
GUG J-F [*S17*]				3.25				2001
SA 93-1 [2]						4.00		537
EN113_13D-1B [2]						0.14	93	755

[1] Analyzed by secondary ionization mass spectrometry at the Department of Terrestrial Magnetism, Carnegie Insitution of Washington, following the techniques of Hauri (*S3*).

[2] Analyzed by electron microprobe and/or Fourier Transform Infrared Spetroscopy at the National Museum of Natural History, Smithsonian Institution, following the techniques of Luhr (*S4*).

Supplemental Data Table 2A. Post-entrapment corrected melt compositions for olivine-hoted melt inclusions

Sample Name	Smithsonian Catalog Number	Type	Location	Olivine Added (%)	Fe^{2+} Added (wt% FeO)	SiO_2	TiO_2	Al_2O_3	Fe_2O_3	FeO	MnO	MgO	CaO	Na_2O	K_2O	P_2O_5	Total	$Fe^{3+}/\sum Fe$	H_2O, wt.%	CO_2, ppm	S, ppm
108153-A	108153	Arc MI	Paricutin, Mexico		0.68	52.12	0.97	16.34	1.46	6.00	0.13	4.92	6.85	3.39	1.05	0.40	93.63	0.18	3.97	294	2483
2A/22/5/92-A	117273-25	Arc MI	Barren Island, Andaman		0.54	52.56	1.15	16.27	2.34	9.00	0.23	4.34	7.23	2.80	0.65	0.14	96.70	0.19	2.88	13	786
2A/22/5/92-B	117273-25	Arc MI	Barren Island, Andaman		0.69	51.19	1.17	16.21	2.43	8.70	0.25	4.18	7.45	3.92	0.64	0.16	96.30	0.20	3.34	19	1019
G98-02		Arc MI	Galunggung, Java	19		47.78	1.11	17.09	1.27	7.32	0.12	10.51	10.96	2.72	0.46	0.12	99.48	0.13	0.21	83	460
05AUNY17_1		Arc MI	Augustine, Aleutians		0.40	48.54	0.66	17.12	2.73	5.75	0.14	4.43	10.46	2.15	0.54	0.17	92.69	0.30	5.29	144	4114
GUG BB		Arc MI	Guguan, Marianas		0.47	44.41	1.09	17.73	3.12	9.18	0.21	5.84	12.05	1.94	0.33	0.09	95.99	0.23	2.79	175	
GUG D		Arc MI	Guguan, Marianas	0		45.70	0.74	18.01	3.38	8.28	0.24	5.44	12.58	1.95	0.30	0.09	96.70	0.27	3.28		1894
GUG DB		Arc MI	Guguan, Marianas		1.89	51.02	1.03	14.52	2.95	11.75	0.25	4.66	7.64	2.73	0.55	0.13	97.23	0.18	2.23		301
GUG J-F		Arc MI	Guguan, Marianas	2	0.24	45.86	0.78	17.78	3.24	9.07	0.25	5.54	12.26	1.94	0.32	0.04	97.08	0.24	3.19		1962
SA 93-1		Arc MI	Sarigan, Marianas	4		52.95	0.53	15.03	2.32	5.44	0.13	4.35	10.57	2.05	0.55	0.03	93.94	0.28	3.85		516
EN113_13D-1B		MORB MI	East Pacific Rise	1		48.20	1.19	18.18	1.33	6.69	0.14	8.21	12.03	3.22	0.01	0.08	99.28	0.15	0.14	92	748

Supplemental Data Table 3. Average $Fe^{+3}/\sum Fe$ ratios and Ba/La for MORB and Mariana trough/arc

Samples	MgO range (wt.%)	Ave. $Fe^{3+}/\sum Fe$	2 σ	Ave. Ba/La	2 σ
Ave. MORB	7.0-7.5	0.16 [1]	0.007	4.37 [2]	0.69
Mariana Tr. <1 wt% H_2O	7.0-7.5	0.15	0.004	6.44 [3]	1.93
Mariana Tr. >1 wt.% H_2O	7.0-7.5	0.17	0.005	11.97 [3]	0.40
Ave. Guguan	4.7-5.9	0.23	0.035	49.66 [4]	7.69

[1] Average $Fe^{3+}/\sum Fe$ compiled from the global MORB data set of (*S20*)

[2] Average Ba/La ratio of East Pacific Rise seamounts from (*S21*)

[3] Average Ba/La ratio for Mariana trough samples analyzed in this study from (*S22*)

[4] Average Ba/La ratio of whole-rock Guguan basaltic lavas from (*S23*)

References

S1. E. Cottrell, K. A. Kelley, A. T. Lanzirotti, R. A. Fischer, *Chemical Geology* (revised (2009)).
S2. N. Shimizu, A. Masuda, U. Tadahide, *INIT REP DSDP* **51-53**, 1113 (1980).
S3. E. Hauri, *Chemical Geology* **183**, 99 (2002).
S4. J. F. Luhr, *Contributions to Mineralogy and Petrology* **142**, 261 (Dec, 2001).
S5. P. Michael, *Earth and Planetary Science Letters* **131**, 301 (1995).
S6. W. G. Melson, T. O'Hearn, E. Jarosewich, *Geochemistry Geophysics Geosystems* **3** (10 April 2002, 2002).
S7. P. J. le Roux, S. B. Shirey, E. H. Hauri, M. R. Perfit, J. F. Bender, *Earth and Planetary Science Letters* **251**, 209 (2006).
S8. C. H. Langmuir, *PetDB Submitted Dataset* (1999).
S9. R. J. Poreda, J.-G. Schilling, H. Craig, *Earth and Planetary Science Letters* **78**, 1 (1986).
S10. S. Newman, E. Stolper, R. J. Stern, *Geochemistry Geophysics Geosystems* **1** (30 May 2000, 2000).
S11. R. F. Gribble, R. J. Stern, S. Newman, S. H. Bloomer, T. O'Hearn, *Journal of Petrology* **39**, 125 (1998).
S12. E. Stolper, S. Newman, *Earth and Planetary Science Letters* **121**, 293 (1994).
S13. J. W. Hawkins, P. F. Lonsdale, J. D. Macdougall, A. M. Volpe, *Earth and Planetary Science Letters* **100**, 226 (1990).
S14. J. F. Luhr, D. Haldar, *Journal of Volcanology and Geothermal Research* **149**, 177 (2006).
S15. K. A. Kelley, E. H. Hauri, T. W. Sisson, *EOS Transactions AGU* **85**, Fall Meet. Suppl. (2004).
S16. M. Zimmer *et al.*, *EOS Transactions AGU* **85**, Fall Meet. Suppl. (2004).
S17. K. A. Kelley *et al.*, *EOS Transactions, AGU* **84**, V41D (2003).
S18. H. Sakai, A. Ueda, D. J. Des Marais, J. G. Moore, *Geochimica et Cosmochimica Acta* **48**, 2433 (1984).
S19. J. C. Alt, W. C. Shanks, III, M. C. Jackson, *Earth and Planetary Science Letters* **119**, 477 (1993).
S20. K. A. Kelley, E. Cottrell, *EOS Transactions AGU*, Fall Meeting Suppl. (2008).
S21. Y. Niu, R. Batiza, *Earth and Planetary Science Letters* **148**, 471 (1997).
S22. J. A. Pearce, R. J. Stern, S. H. Bloomer, P. Fryer, *Geochemistry Geophysics Geosystems* **6**, Q07006 (2005).
S23. T. Elliott, T. Plank, A. Zindler, W. M. White, B. Bourdon, *Journal of Geophysical Research* **102**, 14991 (10 July, 1997, 1997).